

*Proc. of the 61st Fujihara Seminar: Progress in solar/stellar physics with helio- and asteroseismology
ASP Conference Series, Vol. **Volume Number**
ed. H. Shibahashi, M. Takata, & A. E. Lynas-Gray
© **Copyright Year** Astronomical Society of the Pacific*

Helioseismic detection of emerging magnetic flux

Stathis ILONIDIS, Junwei ZHAO, and Alexander G. KOSOVICHEV

*W.W. Hansen Experimental Physics Laboratory, Stanford University, Stanford,
CA 94305-4085, USA*

Abstract. Investigating the properties of magnetic flux emergence is one of the most important problems of solar physics. In this study we present a newly developed deep-focus time-distance measurement scheme which is able to detect strong emerging flux events in the deep solar interior, before the flux becomes visible on the surface. We discuss in detail the differences between our method and previous methods, and demonstrate step-by-step how the signal-to-noise (S/N) ratio is increased. The method is based on detection of perturbations in acoustic phase travel times determined from cross-covariances of solar oscillations observed on the surface. We detect strong acoustic travel-time reductions of an order of 12 – 16 seconds at a depth of 42 – 75 Mm. These acoustic anomalies are detected 1 – 2 days before high peaks in the photospheric magnetic flux rate implying that the average emerging speed is $0.3 - 0.6 \text{ km s}^{-1}$. The results of this work contribute to our understanding of solar magnetism and benefit space weather forecasting.

1. Introduction

Solar magnetic fields are presumably generated by a dynamo action in the deep interior of the Sun and emerge through the convection zone to the photosphere. The properties of magnetic flux emergence are related to some of the most important problems of solar physics: the depth of dynamo, the appearance and evolution of active regions, the formation of sunspots, the initiation of flares and coronal mass ejections, and the 11-year activity cycle. The detection of emerging magnetic flux events in the deep solar interior may improve our understanding of solar magnetism.

Early detection of emerging magnetic structures in the solar interior will also benefit space weather forecasting. Sunspot regions produce flares and coronal mass ejections (CMEs) which may cause power outages as well as interruptions of telecommunication and navigation services. It is important therefore to monitor the subsurface magnetic activity and, if it is possible, to predict the emergence of sunspots as well as the eruptive events associated with them.

There have been several attempts to detect emerging magnetic flux prior to its appearance in the photosphere. Chang et al. (1999) constructed phase-shift maps of Active Region (AR) 7978 using the method of acoustic imaging (Chang et al. 1997) and reported the detection of upward-moving magnetic flux during the development of the active region. Kosovichev et al. (2000) studied, with the time-distance technique (Duvall et al. 1993), the emergence of an active region which appeared on the solar disc on 1998 January 11 and estimated the emerging speed at about 1.3 km s^{-1} . Jensen et al. (2001) analyzed the same active region and found that wave-speed pertur-

bations extend at least 20 Mm below the active region. Kosovichev & Duvall (2008) investigated the emergence of AR 10488 which was observed with the Solar and Heliospheric Observatory (SOHO) Michelson Doppler Imager (MDI) in October 2003. The authors suggest that the active region was formed as a result of multiple flux emergence events. They also found that the emergence was accompanied by strong shearing outflows. Zharkov & Thompson (2008) investigated the emergence of AR 10790 using the same time-distance approach as Kosovichev et al. (2000). They observed regions with sound speed perturbations, presumably related to subsurface emerging flux, and estimated the speed of emerging flux at about 1 km s^{-1} . Komm et al. (2009) found, using a ring-diagram analysis (Hill 1988), that at some depth ranges, the vertical flows show temporal variations that correspond to photospheric variations of the magnetic flux. Hartlep et al. (2011) showed that, under certain conditions, subsurface structures related to emerging magnetic flux can modify the acoustic power observed at the photosphere above them. For a recent review on the dynamics of emerging magnetic flux see Kosovichev (2009).

Recently, Ilonidis et al. (2011) detected significant travel-time perturbations at a depth of about 42 – 75 Mm and showed that these perturbations were associated with magnetic structures that emerged with an average speed of $0.3\text{--}0.6 \text{ km s}^{-1}$ and appeared at the surface 1 – 2 days after the detection of the perturbations. Here, we describe the analysis method in detail and demonstrate step-by-step how the S/N ratio is increased. We also present travel-time maps of 2 emerging flux regions which show the temporal evolution of the detected travel-time anomalies.

2. Data and Method

Doppler observations from MDI onboard SOHO (Scherrer et al. 1995) are used in this work. Each dataset is 8-hours long, tracked with a Carrington rotation rate and remapped to heliographic coordinates using Postel's projection. The datasets are tracked with a spatial resolution of $0.12^\circ \text{ pixel}^{-1}$, a temporal resolution of 1 minute, and a size of 256×256 pixels. Each dataset is then filtered in the Fourier domain and only the oscillation signals with frequencies between 2 – 5 mHz and phase speeds between 92 – 127 km s^{-1} are kept for further processing.

A new deep-focus time-distance measurement scheme is then applied for the computation of the cross-covariances. This measurement scheme introduces 4 modifications to the deep-focus time-distance measurement schemes that were used in previous studies. We discuss these modifications below and we show that they improve the S/N ratio.

The first modification is related to the phase-speed filtering. Phase-speed filters select acoustic waves with the same (or similar) phase speed(s). These waves have the same penetration depth and can be used to investigate properties of the flux emergence at specific depths. The most challenging part in the selection of a phase-speed filter is the determination of the exact shape and width of the filter. Helioseismology usually uses Gaussian phase-speed filters with the width chosen empirically. However, the choice of the shape and/or the width of the phase-speed filter can affect both the signal (travel-time shift caused by an emerging flux event) and the noise (travel-time shifts measured in quiet-Sun regions) levels. Figure 1 shows an example where two phase-speed filters with the same central phase speed are tested in the same emerging-flux and quiet-Sun regions. It turns out that the filter with the lower noise level, estimated by

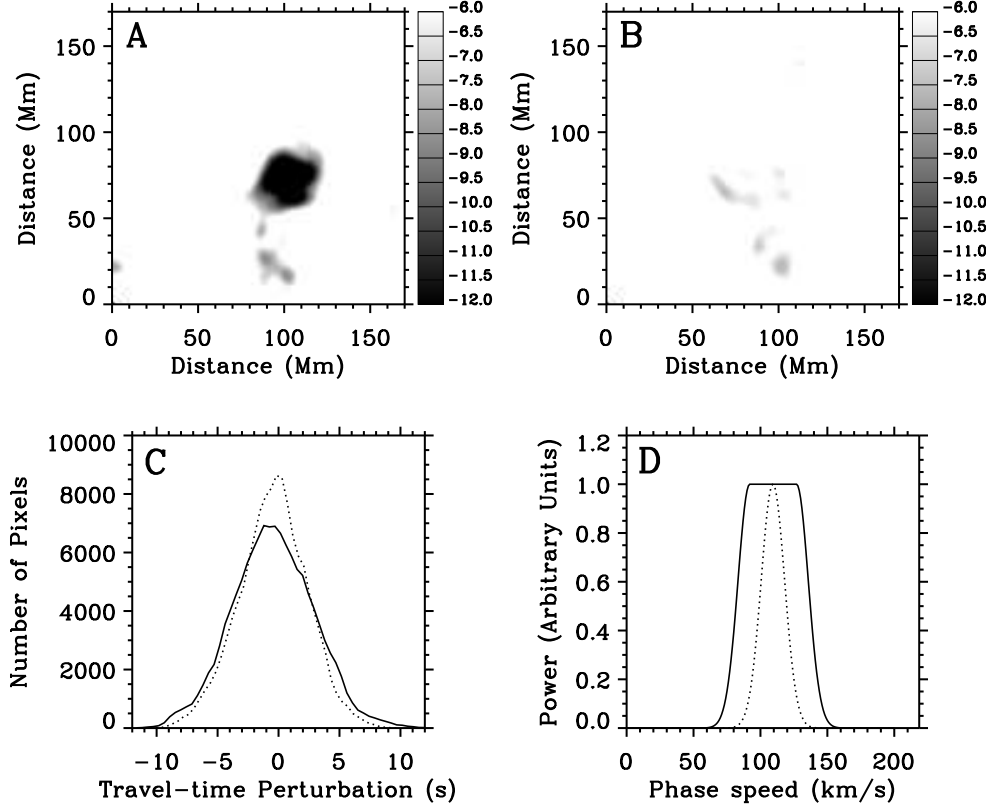


Figure 1. (A) Mean travel-time perturbation map (in seconds) of AR 10488 at a depth of 42 – 75 Mm obtained from an 8-hour dataset centered at 03:30 UT, 26 October 2003. The map was computed using the phase-speed filter shown in panel D with solid line and arcs with a size of 45° and 4 different orientations. The maximum phase travel-time shift is 16.2 s. (B) Same as panel A except that the map was computed using the Gaussian phase-speed filter shown in panel D with a dotted line. The maximum travel-time shift is 7.4 s. (C) Distribution of the travel-time shifts measured in 9 quiet-Sun regions using exactly the same procedure as in panel A (solid line) and exactly the same procedure as in panel B (dotted line). The standard deviations of these measurements is 3.4 s and 2.9 s which yield S/N ratios of 4.8 and 2.6 for the signature detected in panels A and B respectively. (D) The two phase-speed filters used for computation of the travel-time maps in panels A and B.

the quiet-Sun measurements, does not have a higher S/N ratio because of the significant reduction on the signal level. This simple example demonstrates the importance of the optimal phase-speed filter selection. Gaussian phase-speed filters that minimize the noise level and have been widely used in helioseismology may not necessarily maximize the S/N ratio. Here, we choose a Π -shaped filter which selects all the acoustic waves with phase speeds between $92 - 127 \text{ km s}^{-1}$ and drops, outside of this range, as a

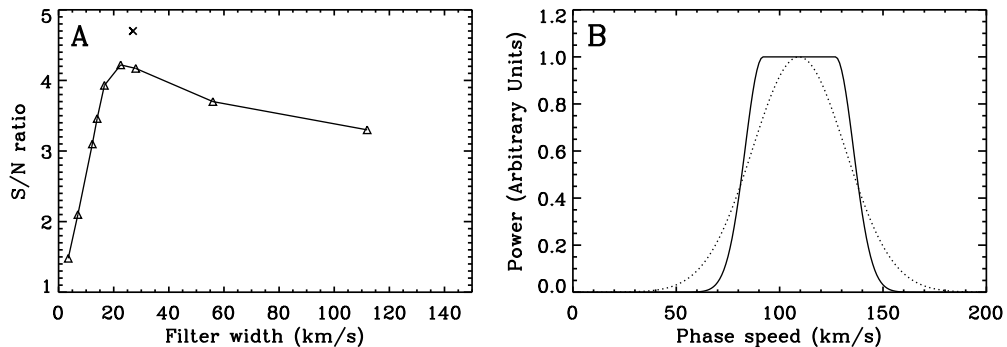


Figure 2. Panel A shows the S/N ratio as a function of the width (standard deviation) of a Gaussian phase-speed filter. The S/N ratios were estimated by analyzing emerging-flux and quiet-Sun regions, as shown in Fig. 1, using the method described there. The cross sign (\times) indicates the S/N ratio of the optimized filter shown in panel B with a solid line which was used for the detection of emerging sunspot regions. This filter has higher S/N ratio than any Gaussian phase-speed filter with the same central phase-speed. The dotted line in panel B shows the Gaussian filter which yields the highest S/N ratio among the Gaussian filters of panel A.

Gaussian function with width (standard deviation) of 8.7 km s^{-1} . The S/N ratio of this phase-speed filter is higher than any Gaussian phase-speed filter with the same central phase-speed (Fig. 2).

The second modification is related to the computation of cross-covariances. According to the previous deep-focus time-distance measurement scheme, an annulus is selected on the solar surface and the oscillation signals at every pair of diametrically opposite points on this annulus are cross-correlated both for positive and negative time lags. The cross-correlation functions are then averaged and the two lags are combined to increase the S/N ratio. Here, we follow a different approach. We select an annulus on the solar surface and devide it into an even number of arcs. We average the oscillation signal inside each arc and compute cross-covariances between the averaged signals of every pair of diametrically opposite arcs. The cross-covariance functions are computed for both positive and negative time lags. These functions are then averaged and the two lags are combined to increase the S/N ratio. Ilonidis and Zhao (2011) used this procedure, with an arc size of 90° , to measure the coefficients of absorption, emissivity reduction, and local suppression inside sunspots.

Averaging the oscillation signal over an arc allows us to use many different arc configurations for the computation of cross-covariances. This is the third modification to the previous measurement scheme. In the new scheme, both the arc size and the arc orientation are free parameters that can be chosen to maximize the S/N ratio. We select arcs of 5 different sizes and for each arc size, we use 4 orientations. The arcs have a size of 25.7° , 30° , 36° , 45° and 60° (so that the annuli are divided into 14, 12, 10, 8 and 6 arcs respectively). We select the 4 orientations starting from an arbitrarily oriented configuration with N arcs in such a way that every other configuration with N arcs is produced from the previous one by a rotation of $N/4$ degrees. In total, we

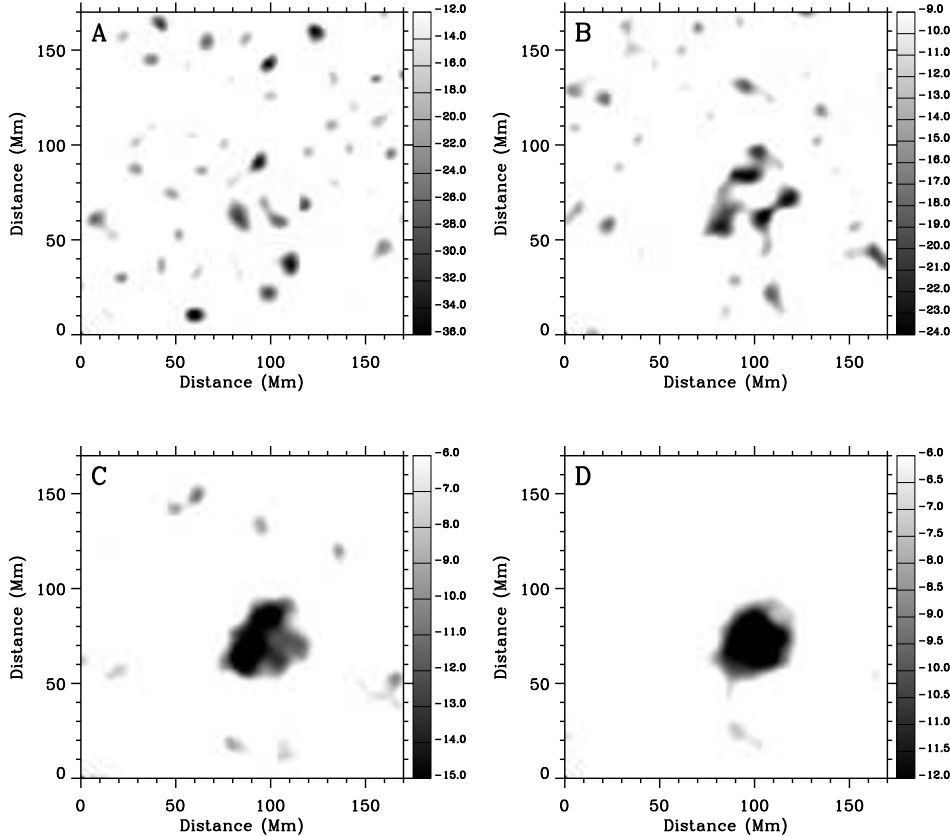


Figure 3. Demonstration of a step-by-step improvement of the S/N ratio in the mean travel-time perturbation maps. The emerging-flux region is the same as in Fig. 1. Each panel introduces one or more modifications to the previous deep-focus time-distance measurement scheme: (A) The previous method: point-to-point computation of cross-covariance function with a Gaussian phase-speed filter with width (standard deviation) of 12.3 km s^{-1} using 9 focus depths between 54 and 62 Mm. The S/N ratio is rather low. (B) Same as in panel A but with 2 modifications: the map was computed using the new filter (solid line of Fig. 2 B) and 31 focus depths between 42 and 75 Mm. The S/N ratio is 3.2. (C) Same as in panel B but with one additional modification: the cross-covariances are computed after averaging the oscillation signal over arcs with a size of 25.7° . The S/N ratio is 3.9. (D) Same as in panel C but with one additional modification: the cross-covariances are computed using the 20 arc configurations described in the text. The S/N ratio is 4.9.

use 20 different arc configurations. The cross-covariances computed from all these configurations are combined to increase the S/N ratio.

The last modification is related to the depth range of our measurements. The goal of a helioseismic study is often to map perturbations in the solar interior. The oscillation signals which are selected and cross-correlated on the solar surface correspond

to the starting and ending points of acoustic wave paths which, in the ray-path approximation, are focused on a single point deep below the photosphere. Therefore, perturbations in the acoustic travel time essentially map local inhomogeneities around the focal point. Here, we combine the cross-covariances obtained from 31 travel distances (corresponding to 31 focus depths) in order to increase the S/N ratio. The total depth range of our measurements is 42 – 75 Mm. So the travel-time maps presented here are sensitive to acoustic anomalies in this wide range of depths. We should note that cross-covariances obtained for the different travel distances are averaged after appropriate time shifts based on quiet-Sun measurements.

We compute the cross-covariances using the method described above with the new optimal phase-speed filter, the 20 arc configurations and the 31 travel distances, and we combine these cross-covariances in order to increase the S/N ratio. The final cross-covariance is fitted with a Gabor wavelet (Kosovichev and Duvall 1996) to obtain the acoustic phase travel time of one cross-covariance peak. This procedure is repeated for all the pixels in the observed area, and an acoustic phase travel-time map is constructed. We should note that the definition of phase travel time may be different in other local helioseismology methods and this difference should be taken into account when comparing results obtained with different methods.

3. Results

We present travel-time maps of two emerging flux regions. Active Region (AR) 10488 was one of the largest active regions of Solar Cycle 23. It started emerging on the solar disc at 09:30 UT, 26 October 2003, about 30° East of the central meridian. The emergence showed a steep increase in the magnetic flux rate with a high peak at about 08:00 UT, 27 October. Travel-time maps of this active region at a depth of about 42–75 Mm are shown in Fig. 4. A strong subsurface travel-time anomaly started developing at about 23:30 UT, 25 October (the time always corresponds to the mid-point of an 8-hour dataset used for cross-covariance computations), 10 hours before the start of emergence. This feature increased in size and strength during the next 4–5 hours and then gradually weakened, over a period of 3-4 hours, until the signal fell below the noise level. This feature had a maximum travel-time perturbation, estimated by our method, of 16.3 s relative to the quiet Sun. No other strong travel-time anomalies were detected at this location during the next 1 – 2 days. It should be pointed out that the development and decay of this strong subsurface travel-time anomaly happened several hours before the start of emergence at the surface. The magnetic field at that time and until the start of emergence was very quiet, and no signature of magnetic field emergence was visible in the magnetograms. Magnetic field observations as well as plots of the total flux and the flux rate of this active region can be found in Ilonidis et al. (2011).

AR 8164, which was smaller and less active than AR 10488, started emerging in the northern solar hemisphere at about 04:00 UT, 23 February 1998. The magnetic flux rate at the surface showed initially a steep increase followed by a high peak at about 08:00 UT, 24 February. Figure 5 shows travel-time maps of this active region before and during the start of emergence. A strong travel-time anomaly appeared first in the travel-time maps at 23:00 UT, 22 February and persisted for about 7 hours. This feature had a maximum travel-time perturbation of about 14.0 s.

Our analysis method was also applied to 9 quiet-Sun regions with no emerging flux events in order to estimate the noise level of our measurements. The analysis method

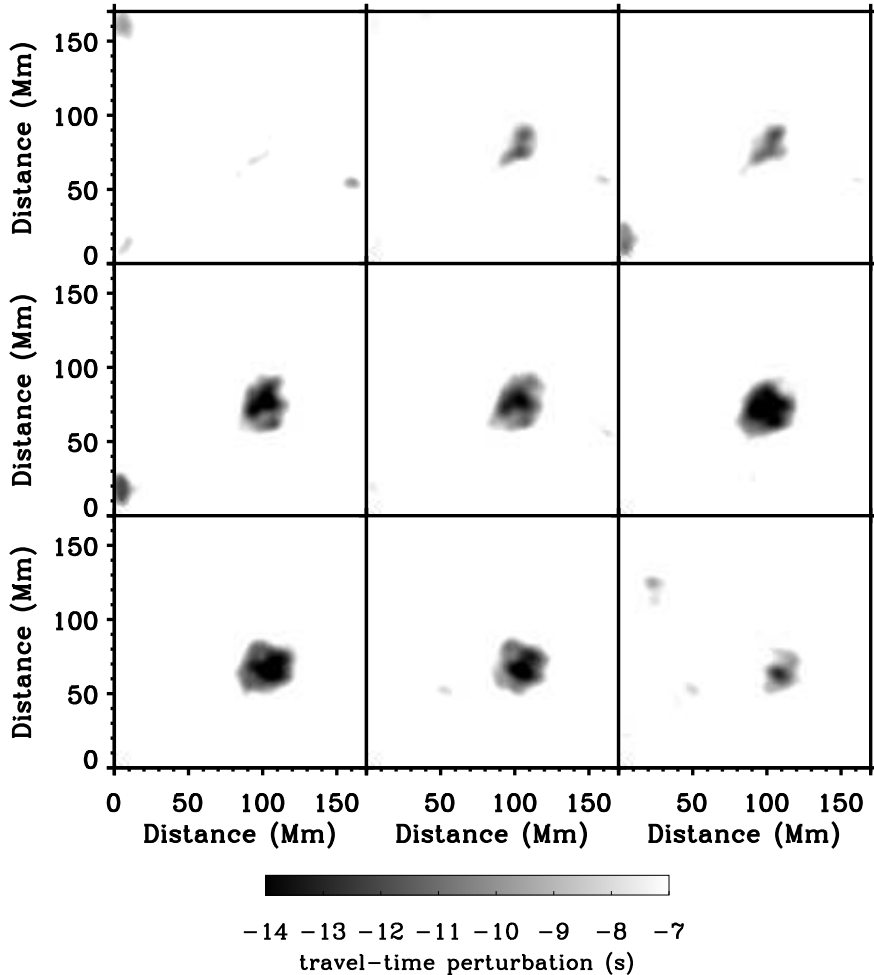


Figure 4. Mean travel-time perturbation maps of AR10488 at a depth of 42 – 75 Mm obtained from 8-hour MDI Doppler-shift datasets. From top left to bottom right, the maps are centered at 22:30 UT 25 October 2003, 23:30 UT, 00:30 UT 26 October 2003, 01:30 UT, 02:30 UT, 03:30 UT, 04:30 UT, 05:30 UT, 06:30 UT. A strong travel-time anomaly appeared before the start of emergence and persisted for about 8 hours.

(measurement scheme, phase-speed filtering, fitting etc) was exactly the same as for the emerging flux regions. The quiet-Sun measurements showed no significant travel-time perturbations. The standard deviation of these measurements was 3.3 s which yields a S/N ratio for ARs 10488 and 8164 of 4.9 and 4.2 respectively. The travel-time shifts measured in quiet regions can be caused by the stochastic realization noise of solar oscillations, small errors in the fitting of the cross-covariance function, or by physical effects such as thermal perturbations and weaker magnetic fields in the convection zone.

The detection of the strong signals in Figs. 4 and 5, which persist for about 8 hours, does not necessarily mean that the flux emergence takes place for only 8 hours. Perhaps a more appropriate interpretation is that the flux is strong enough to cause

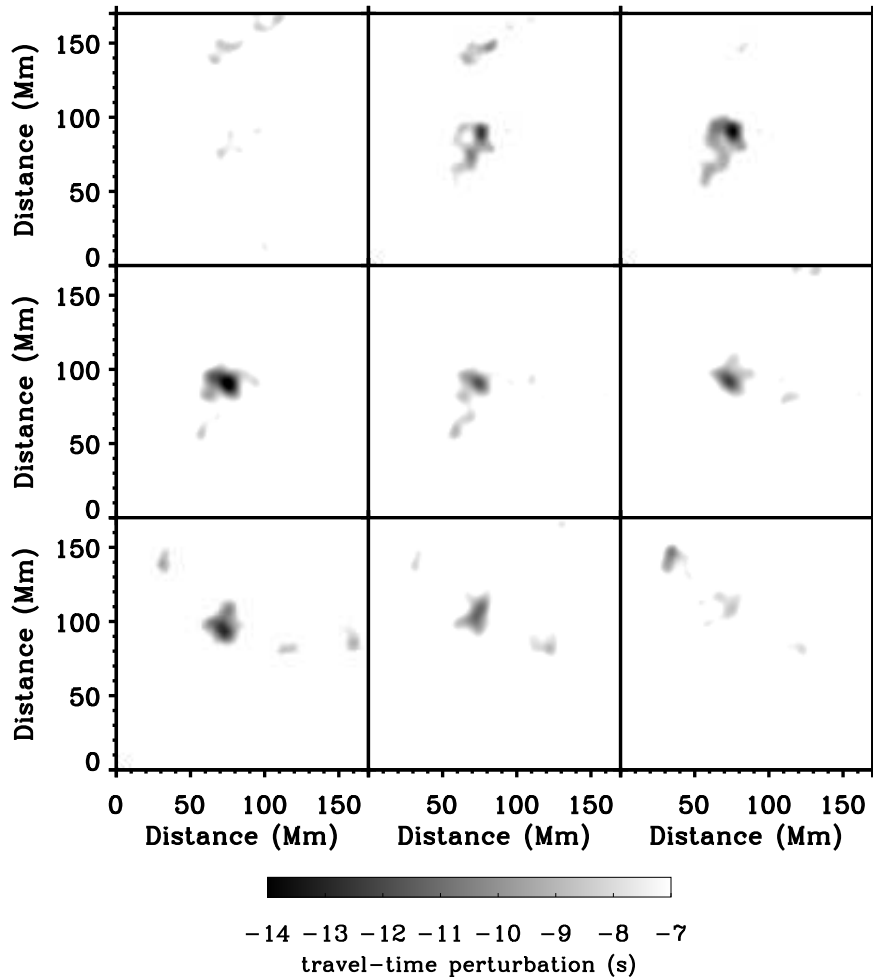


Figure 5. Mean travel-time perturbation maps of AR 8164 at a depth of 42–75 Mm obtained from 8-hour MDI Doppler-shift datasets. From top left to bottom right, the maps are centered at 22:00 UT 22 February 1998, 23:00 UT, 00:00 UT 23 February 1998, 01:00 UT, 02:00 UT, 03:00 UT, 04:00 UT, 05:00 UT, 06:00 UT. A strong travel-time anomaly appeared before the start of emergence and persisted for about 7 hours.

detectable travel-time shifts by this method only for about 8 hours. The detected travel-time perturbations correspond, most probably, to strong emerging flux events at a depth of 42–75 Mm which reach the surface 1–2 days after the detection and cause high peaks in the photospheric flux rate. The magnetic flux observations at the surface and our helioseismic measurements confirm this scenario. The strongest travel-time anomalies of ARs 10488 and 8164 were detected about 28.5 and 32 hours respectively before the highest peaks in the corresponding flux rates. The magnetic field of AR 10488, which was stronger (and therefore more buoyant) than AR 8164 caused larger travel-time shifts and emerged faster in the photosphere. The study of 2 other emerging flux events, presented in Ilonidis et al. (2011), confirm this scenario as well. The estimated

average emerging speed of about $0.3 - 0.6 \text{ km s}^{-1}$ is consistent with estimates from numerical simulations (Fan, 2009).

The horizontal wavelength of the acoustic waves employed in this study is about 35 Mm at 3.5 mHz. The large wavelength poses limits on both the size of structures that can be resolved and the accuracy of their location. The amplitude of the travel-time perturbations is larger than theoretical estimates based on numerical simulations of emerging flux tubes (Birch et al. 2010). These estimates were derived though with a very different method, and at this point it is not known if the discrepancies are caused by the differences in the two methods. In addition, the interpretation of the detected signals is not a simple task because the nature of the travel-time anomaly is not known. Observational studies on the interaction of acoustic waves with magnetic fields (Zhao 2011) show that magnetic fields cause complicated changes in the cross-covariance function and not simple uniform shifts. Perhaps, a more detailed study of the cross-covariance function may give some hints about the nature of the detected perturbations.

Monitoring and predicting solar magnetic activity is a useful tool for space weather forecasts. Sunspot regions can either emerge from the solar interior or rotate into our view from the Sun's East limb. Our method combined with continuous observations from the Helioseismic and Magnetic Imager onboard the Solar Dynamics Observatory and the far-side imaging technique (Lindsey & Braun 2000; Zhao 2007; Ilonidis et al. 2009) may allow anticipation of large sunspot regions days before they appear on the solar disc.

Acknowledgments. The authors thank P. Scherrer and T. Duvall for discussions and useful comments.

References

- Birch, A., Braun, D. C., & Fan, Y. 2010, ApJ, 723, L190
 Chang, H.-K., Chou, D.-Y., Labonte, B., & The TON Team 1997, Nature, 389, 825
 Chang, H.-K., Chou, D.-Y., Sun, M.-T. 1999, ApJ, 526, L53
 Duvall, T. L., Jr., Jefferies, S. M., Harvey, J. W., & Pomerantz, M. A. 1993, Nature, 362, 430
 Fan, Y. 2009, Living Rev. Solar Phys., 6, 4
 Hartlep, T., Kosovichev, A. G., Zhao, J., Mansour, N. N. 2011, Solar Phys., 268, 321
 Hill, F. 1988, ApJ, 333, 996
 Ilonidis, S., Zhao, J. 2011, Solar Phys., 268, 377
 Ilonidis, S., Zhao, J., Hartlep, T. 2009, Solar Phys., 258, 181
 Ilonidis, S., Zhao J., & Kosovichev, A. 2011, Science, 333, 993
 Jensen, J. M., Duvall, T. L., Jr., Jacobsen, B. H., & Christensen-Dalsgaard, J. 2001, ApJ, 553, L193
 Komm, R., Howe, R., & Hill, F. 2009, Solar Phys., 258, 13
 Kosovichev, A. G. 2009, Space Sci. Rev., 144, 175
 Kosovichev, A. G., Duvall, T. L., Jr. 1996, in Proc. SCORe'96 Workshop: Solar Convection and Oscillations and Their relationship, ed. F. P. Pijpers, J. Christensen-Dalsgaard, & C. S. Rosenthal, (Dordrecht: Kluwer), 241
 Kosovichev, A. G. & Duvall, T. L., Jr. 2008, ASP Conf. Series 383, 59
 Kosovichev, A. G., Duvall, T. L., Jr., & Scherrer, P. H. 2000, Solar Phys., 192, 159
 Lindsey, C., & Braun, D. C. 2000, Science, 287, 1799
 Scherrer, P. H., Bogart, R. S., Bush, R. I. et al. 1995, Solar Phys., 162, 129
 Zhao, J. 2007, ApJ, 664, L139
 Zhao, J., Kosovichev, A. G., & Ilonidis, S. 2011, Solar Phys., 268, 429
 Zharkov, S. & Thompson, M. J. 2008, Solar Phys., 251, 369